













Cite this: *Mater. Horiz.*, 2017,
4, 900Received 19th April 2017,
Accepted 23rd June 2017

DOI: 10.1039/c7mh00244k

rsc.li/materials-horizons

Origin of the high oxygen reduction reaction of nitrogen and sulfur co-doped MOF-derived nanocarbon electrocatalysts†

Zhongxin Song, ^a Weiwei Liu, ^b Niancai Cheng, ^a
Mohammad Norouzi Banis, ^a Xia Li, ^a Qian Sun, ^a Biwei Xiao, ^a
Yulong Liu, ^a Andrew Lushington, ^a Ruying Li, ^a Limin Liu ^{*b} and
Xueliang Sun ^{*a}

Developing an economical, highly active and durable material to replace the conventional, expensive noble metal electrocatalyst is an important milestone in the development of fuel cell technology. Nanocarbon materials are considered as promising catalysts toward the oxygen reduction reaction (ORR) in fuel cells, due to their reasonable balance between low-cost, long-life durability and high catalytic activity in alkaline media. In this work, we present the fabrication of N,S-co-doped nanocarbon derived from a metal-organic framework (MOF) precursor for use as an electrocatalyst towards ORR. High resolution transmission electron microscopy (HRTEM) mapping demonstrates the uniform distribution of N and S atoms into the nanocarbon skeleton. The nitrogen absorption-desorption isotherms indicate that the MOF-derived N,S-co-doped nanocarbon has a high specific surface area ($2439.9 \text{ m}^2 \text{ g}^{-1}$) and a porous structure. Importantly, the N,S-co-doped nanocarbon exhibits higher catalytic activity toward ORR, better long-term stability and methanol tolerance than commercial Pt/C catalyst. First-principles calculations demonstrate that the remarkable electrochemical properties of N,S-co-doped nanocarbon are mainly attributed to the synergistic effect from the N and S dopants. Moreover, for the first time, it is revealed that the N,S-coupled dopants in nanocarbon can create active sites with higher catalytic activity for ORR than the isolated N and S-dopants. This finding on the structure-performance relationship of the co-doped nanocarbon provides guidelines for the design of high performance electrocatalysts.

Introduction

With remarkable efficiency, high energy density and negligible emission of harmful gases, the polymer electrolyte membrane fuel cell (PEMFC) is considered to be a green technology that

Conceptual insights

Although the newly-developed N-doped graphene represents a promising group of candidates to enhance the catalytic performance, the improvement in catalytic activity toward the oxygen reduction reaction (ORR) is still limited owing to the low content of the active sites. To overcome the limitations of the conventional N-doped carbon electrocatalysts, we innovate here the highly porous N,S-co-doped MOF-nanocarbon constructed with high loading of active sites. Moreover, rather than focusing on only the catalytic activity, the active sites which lead to the ORR performance are elucidated from the aspects of both an electrochemical experiment and first-principles calculations. For the first time, this work provides an insight into the relationship between the doping-structure and performance. It was found that the N,S-co-doped nanocarbon with N and S couples doped on the same C atom creates active carbon sites with higher activity. Due to the synergistic effect of the coupled-N,S dopants, the N,S-couple-doped carbon sites provide a high electron density to the adsorbed O_2 and make the ORR take place easily. These findings will be of great significance for the rational design of a new-generation of nanocarbon electrocatalysts.

meets the energy requirement for future electrical vehicles and portable electronics.¹ Unfortunately, a major limitation for the low-temperature PEMFCs is the kinetically-sluggish oxygen reduction reaction (ORR) at the cathode, which requires a large amount of catalysts to reach the adequate energy output.²⁻⁴ The state-of-the-art high-performance catalysts for ORR are the noble metal Pt-based catalysts.⁵⁻¹⁰ However, Pt catalysts suffer from several issues including high cost, poor stability, the crossover effect and CO poisoning.¹ These bottlenecks hamper the widespread commercialization of PEMFCs. Therefore, it is highly desirable to replace the conventional, expensive catalysts with non-noble metal electrocatalysts that have all the characteristics of high activity, low cost and long-term stability. Recently, the nanocarbon has attracted much attention as an alternative catalyst due to its reasonably low cost, high activity, as well as its unique physical and chemical characteristics. Conventional nanocarbons like carbon black and carbon nanotubes generally exhibit an insufficient catalytic activity toward ORR in fuel cell applications. Several approaches have been

^a Department of Mechanical and Materials Engineering, University of Western Ontario, London, ON, N6A 5B9, Canada. E-mail: xsun@eng.uwo.ca

^b Beijing Computational Science Research Center, Beijing 100084, China. E-mail: limin.liu@csrc.ac.cn

† Electronic supplementary information (ESI) available. See DOI: 10.1039/c7mh00244k

investigated to modify nanocarbons in a way that enhances their catalytic activity. The chemical modification of nanocarbons is especially found to be an effective way of improving their intrinsic activity.^{11–14} In particular, heteroatom-doping, such as doping nanocarbons with nitrogen (N),^{15–17} boron (B),¹⁸ sulfur (S),¹⁹ and/or phosphorus (P),^{20–22} has been reported as an excellent strategy for adjusting the surface polarity and the electronic properties of nanocarbons. The electronegative-N-doped nanocarbon induces the atomic charge density and the spin density redistribution, which consequently promotes the oxygen adsorption and reduction.²³ Moreover, recent pioneering work revealed that binary or ternary-co-doped nanocarbons possess a superior catalytic activity compared to single doped-nanocarbons due to the synergistic effect. The synergistic effect, arising from atomic charge and spin-density change, is favorable for O₂ reduction and electron transfer; this contributes to the enhanced ORR activity.^{24–28}

The metal-organic framework (MOF) is an extensive class of crystalline materials with ultrahigh porosity and enormous surface area, and it has attracted great interest in the field of catalysis.^{29,30} Apart from its direct use, MOF has also been found to be useful as a sacrificial precursor and a template to fabricate various functional nanomaterials.^{30–34} By delicately designing the MOF precursor and with careful post treatment, the benefits of high porosity and catalytic activity of a MOF can be fully transferred into a MOF-derived nanomaterial. For example, a high surface area N-doped nanocarbon derived from the ZIF-8 precursor was shown to have abundant N-doping sites and excellent catalytic activity.^{35,36} Although some newly developed N-doped-nanocarbons have shown performance, the improvement in the ORR catalytic activity has still been very limited due to the low amounts of the active sites. Thus, it is imperative to design a nanocarbon electrocatalyst with high loading of active sites. Before that, to gain an insight into the active sites that lead to the ORR performance is a significant challenge to be overcome.

Here, we report a novel strategy to fabricate N,S-co-doped nanocarbons as catalysts for ORR through adjusting the pore structure and active sites of the MOF-derived nanocarbon. The N,S-co-doped nanocarbon is synthesized using MOF as a solid precursor, followed by carbonization and pore size design, then

further co-doping sulfur to generate more active sites. In our design, the typical Zn-based zeolitic imidazolate framework of ZIF-8 is selected as a template/precursor due to its high content of N-containing organic ligands, and its easy removal of the Zn species at a high temperature. The resulting N,S-co-doped nanocarbon demonstrates a high catalytic activity toward ORR, remarkable long-term stability and strong methanol tolerance in alkaline media. First-principles calculations prove that N,S-co-doped nanocarbons possess enhanced ORR activity compared to N-doped carbon. More importantly, this work for the first time reveals that the N,S-coupled dopants can create active sites with higher activity than the isolated N and S dopants.

Results and discussion

The fabrication of the integrated N,S-co-doped nanocarbon based on the MOF concept is illustrated in Fig. 1. First, the ZIF-8 precursor, with an ordered rhombic dodecahedral morphology, is synthesized at the average particle size of 80 nm (Fig. S1, ESI[†]). After carbonization at 1000 °C, the ZIF-8 crystals are converted into porous N-doped nanocarbon (ZIF-C). Subsequently, under thermal treatment with ammonia gas (NH₃), a much rougher surface is formed on the derived NH₃-C-x particles compared to ZIF-C. The SEM images indicate that ZIF-C (Fig. S2, ESI[†]) and NH₃-C-7 nanocarbons (Fig. 2(a)) fully inherit the morphology and particle size of the ZIF-8 precursor, without framework collapse during the carbonization and NH₃ treatment. A rough surface of NH₃-C-7 after NH₃ treatment suggests that NH₃ may act as a surface modifier, similar to traditional activating agents such as KOH³⁷ and CO₂,³⁸ to etch carbon or oxygen atoms from the nanocarbon framework and tune the porous structure.^{39,40} Finally, the as-proposed N,S-co-doped nanocarbon (N,S-NH₃-C-7) is developed by doping S into the NH₃-C-7 carbon skeleton. As indicated from the SEM images, there is a minimal change in the particle size between nanocarbons of NH₃-C-7 (Fig. 2(a)) and N,S-NH₃-C-7 (Fig. 2(b)). The local structure and composition of the as-prepared N,S-NH₃-C-7 is further confirmed by HRTEM. As shown in Fig. 2(c),

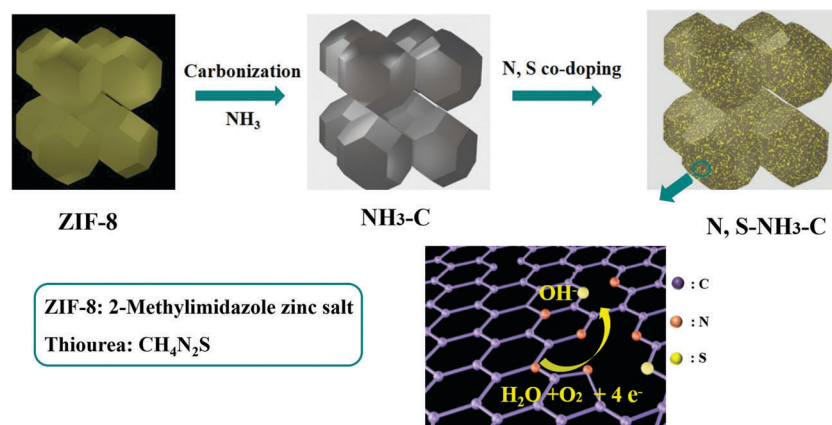


Fig. 1 Schematic illustration of the fabrication of the N,S-co-doped nanocarbon as the electrocatalyst toward ORR. The ZIF-8 precursor and thiourea are used as C/N and S precursors, respectively.

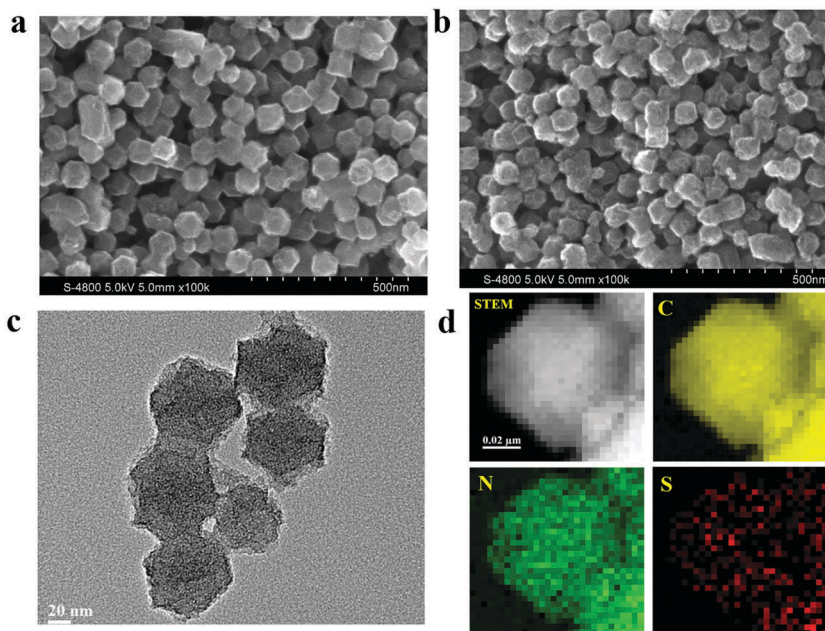


Fig. 2 SEM images of (a) $\text{NH}_3\text{-C-7}$ and (b) $\text{N,S-NH}_3\text{-C-7}$; (c) TEM image of $\text{N,S-NH}_3\text{-C-7}$; (d) STEM images of $\text{N,S-NH}_3\text{-C-7}$ and EELS mapping of C, N, and S elements.

it can be clearly noted that the $\text{N,S-NH}_3\text{-C-7}$ nanocarbon has a polyhedral morphology with a rough surface, which is consistent with the observations noted by SEM analysis. In addition, the electron energy loss spectroscopy (EELS) elemental chemical mapping (Fig. 2(d)) reveals the uniform distribution of elemental carbon, nitrogen, and sulfur in $\text{N,S-NH}_3\text{-C-7}$. This confirms that heteroatoms of nitrogen and sulfur are successfully doped into the carbon skeleton.

The physical properties of the as-prepared nanocarbons are further investigated by XRD and Raman spectroscopy. The XRD patterns of ZIF-C, $\text{NH}_3\text{-C-7}$ and $\text{N,S-NH}_3\text{-C-7}$ are shown in Fig. 3(a). These patterns display two broad peaks at around 26° and 43° , corresponding to the characteristic carbon (002) and (100)/(101) diffractions, respectively. Additionally, no

diffraction peaks of Zn/ZnO impurities could be observed, which means most of the Zn species have been removed during high temperature carbonization. Fig. 3(b) presents the Raman spectra obtained for the nanocarbons. A typical D band (1350 cm^{-1}) resulting from in-plane imperfections of disordered carbon, and a G band (1580 cm^{-1}) resulting from the stretching mode of highly ordered graphitic carbon, is observed for all the samples. Raman spectra are sensitive to subtle structural variations in nanocarbons and the band intensity ratio (I_D/I_G) can reflect the defect generation or defect disappearance on the carbon matrix. A lower I_D/I_G ratio suggests less defects and therefore a higher structural quality.⁴¹ Interestingly, the I_D/I_G ratio for ZIF-C ($I_D/I_G = 0.9$) is lower than that found for $\text{NH}_3\text{-C-7}$ ($I_D/I_G = 1.13$), indicating that the modification of graphitic carbon occurs during the NH_3 treatment process.

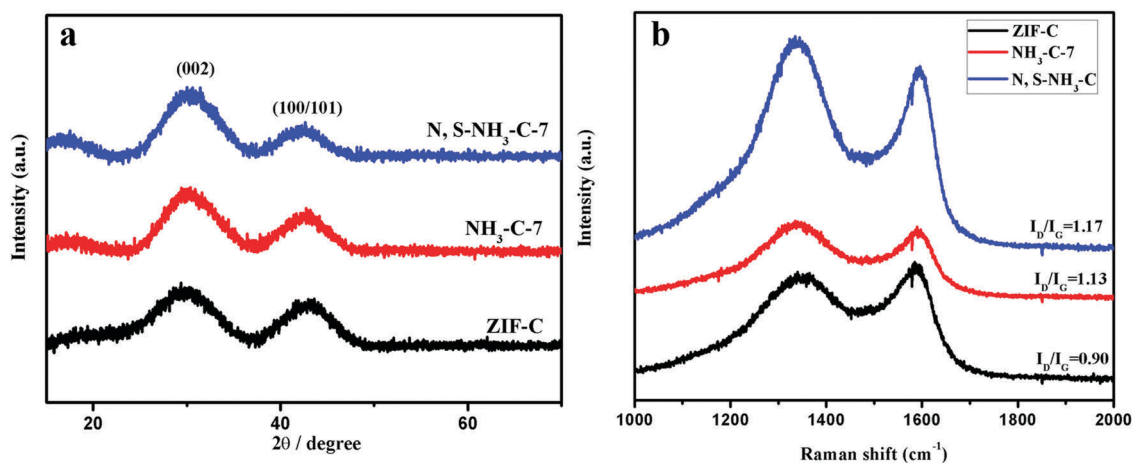


Fig. 3 (a) XRD patterns and (b) Raman spectra of the nanocarbons of ZIF-C, $\text{NH}_3\text{-C-7}$ and $\text{N,S-NH}_3\text{-C-7}$.

In particular, when the exposure time of NH_3 is extended from 3 min to 7 min, there is a gradual increase in the $I_{\text{D}}/I_{\text{G}}$ ratio, from 1.03 to 1.13 (Fig. S3, ESI[†]). This further confirms that the increased duration of NH_3 gas exposure results in the generation of additional defective sites. Therefore, the N-doped nanocarbon of $\text{NH}_3\text{-C-7}$ with high defects is optimized for further S-doping to produce the co-doped nanocarbon of N,S- $\text{NH}_3\text{-C-7}$. A higher $I_{\text{D}}/I_{\text{G}}$ ratio (1.17) found for N,S- $\text{NH}_3\text{-C-7}$ implies that an increased number of heteroatom doping sites (N-doped-C, S-doped-C, NS-coupled-C) can be created on the N,S- $\text{NH}_3\text{-C-7}$ nanocarbon. The large numbers of active doping sites are anticipated to accelerate the ORR process.

The pore structure of catalyst materials plays a significant role in promoting the ORR activity as an appropriate pore size is essential for the diffusion of smooth reactants (O_2 , $-\text{OH}$) and rapid mass transport.⁴² Thus, the impact of NH_3 etching on the textural properties of the MOF-derived nanocarbon is studied by nitrogen absorption/desorption isotherms. The specific surface area and pore size distribution of all synthesized nanocarbons as well as textural properties are shown in Fig. 4 and Table 1, respectively. Generally, at low partial pressures ($P/P_0 < 0.1$), a significant uptake in the isotherms indicates that the MOF-derived nanocarbons exist in the microporous structure (pore size < 2 nm). The hysteresis of desorption between the partial pressures P/P_0 of 0.5–1.0 suggests the presence of mesopores (pore size of 2–50 nm) in $\text{NH}_3\text{-C-}x$ nanocarbons.⁴³ As illustrated in Fig. 4(a), the specific surface area of ZIF-C is only $852.5 \text{ m}^2 \text{ g}^{-1}$. After NH_3 treatment, it increases to $1926.8 \text{ m}^2 \text{ g}^{-1}$, $2276.8 \text{ m}^2 \text{ g}^{-1}$ and $2439.9 \text{ m}^2 \text{ g}^{-1}$, for $\text{NH}_3\text{-C-3}$, $\text{NH}_3\text{-C-5}$ and $\text{NH}_3\text{-C-7}$, respectively. The isotherms are further analyzed using the Barrett–Joyner–Halenda (BJH) and the t -plot method to fit the pore size distribution and micropore volume, respectively. In Fig. 4(b), the samples of ZIF-8 and ZIF-C exhibit a narrow micropore size distribution, centered at ~ 1.8 nm, suggesting that the major pores in ZIF-8 and ZIF-C are micropores; they have a pore volume of $0.80 \text{ cm}^3 \text{ g}^{-1}$ and $0.52 \text{ cm}^3 \text{ g}^{-1}$ (Table 1), respectively. It is interesting to note that there is an increase in pore volume from $1.23 \text{ cm}^3 \text{ g}^{-1}$ to $1.69 \text{ cm}^3 \text{ g}^{-1}$ observed for $\text{NH}_3\text{-C-3}$ and $\text{NH}_3\text{-C-7}$ after NH_3 treatment. Meanwhile, NH_3 treatment of the nanocarbon develops the micropores into mesopores, with an increase in the mesopore volume of up to 88.6% for $\text{NH}_3\text{-C-7}$. Given the results presented by SEM, HRTEM and N_2 absorption/desorption isotherms, NH_3 treatment certainly plays a significant role in tuning the textural properties of MOF-derived nanocarbons.

To analyze the chemical bonding states of the doped nanocarbon, XPS measurements are carried out on N,S- $\text{NH}_3\text{-C-7}$, $\text{NH}_3\text{-C-7}$ and ZIF-C. In Fig. S4 (ESI[†]), the XPS survey spectra of N,S- $\text{NH}_3\text{-C-7}$ show that both N (~ 5.4 at%) and S (~ 0.3 at%) atoms are successfully incorporated into the nanocarbon framework. The N concentration in N,S- $\text{NH}_3\text{-C-7}$ (~ 5.4 at%) is almost the same with the N content found in $\text{NH}_3\text{-C-7}$ (~ 5.1 at%) and ZIF-C (~ 5.0 at%). This means that NH_3 treatment does not dope more N elements on MOF-derived nanocarbons. The high resolution $\text{N}1\text{s}$ spectra of N,S- $\text{NH}_3\text{-C-7}$, $\text{NH}_3\text{-C-7}$ and ZIF-C in Fig. 5(a) display the presence of four nitrogen species:

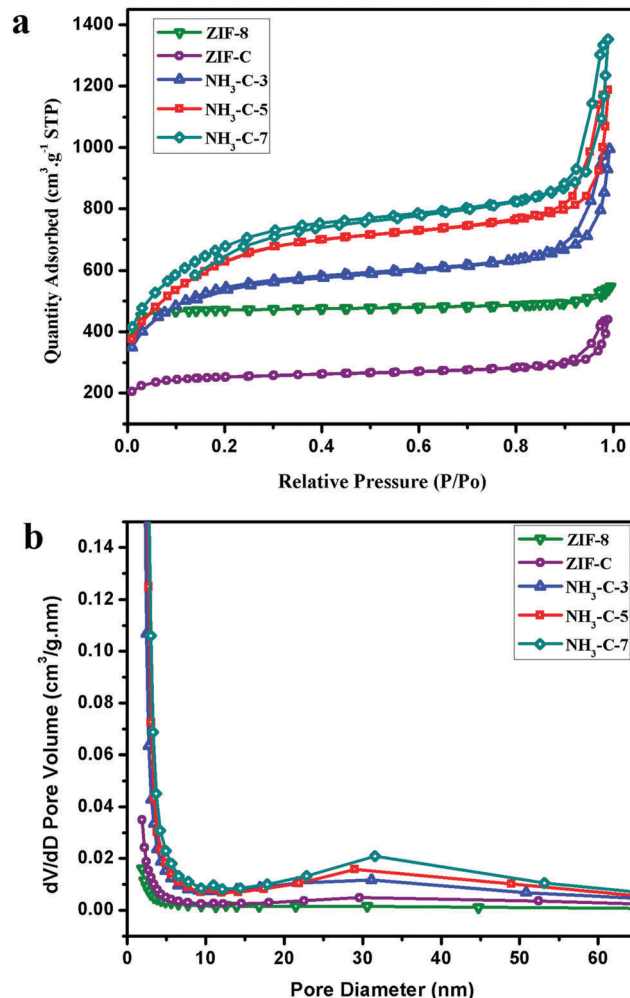


Fig. 4 (a) N_2 adsorption–desorption isotherms and (b) pore size distribution data obtained by the Barrett–Joyner–Halenda (BJH) method of ZIF-8, ZIF-C and $\text{NH}_3\text{-C-}x$.

Table 1 Surface area and pore volume characteristics of ZIF-8, ZIF-C and $\text{NH}_3\text{-C-}x$

Sample	Surface area ($\text{m}^2 \text{ g}^{-1}$)	Total pore volume ($\text{m}^3 \text{ g}^{-1}$)	Micropore volume ($\text{m}^3 \text{ g}^{-1}$)	$V_{\text{meso}}/V_{\text{total}}$ (%)
ZIF-8	1568.8	0.80	0.70	12.5
ZIF-C	852.5	0.52	0.31	40.7
$\text{NH}_3\text{-C-3}$	1926.8	1.23	0.35	72.0
$\text{NH}_3\text{-C-5}$	2276.8	1.43	0.12	80.6
$\text{NH}_3\text{-C-7}$	2439.9	1.69	0.19	88.6

pyridinic-N (~ 398.3 eV), pyrrolic-N (~ 399.5 eV), graphitic-N (~ 401.0 eV) and oxidized-N (~ 404.1 eV). Notably, NH_3 treatment plays a role in adjusting the relative quantities of pyridinic-N and graphitic-N. In Fig. 5(b), the proportions of pyridinic-N increased while those of graphitic-N decreased in $\text{NH}_3\text{-C-7}$ and N,S- $\text{NH}_3\text{-C-7}$ compared to those of ZIF-C which were not treated with NH_3 . Based on the XPS analysis, it is found that the NH_3 heating process helps in the conversion of graphitic-N to pyridinic-N. Previous research has established that pyridinic-N with planar configurations is active toward ORR.⁴⁴ In contrast, graphitic-N atoms, which

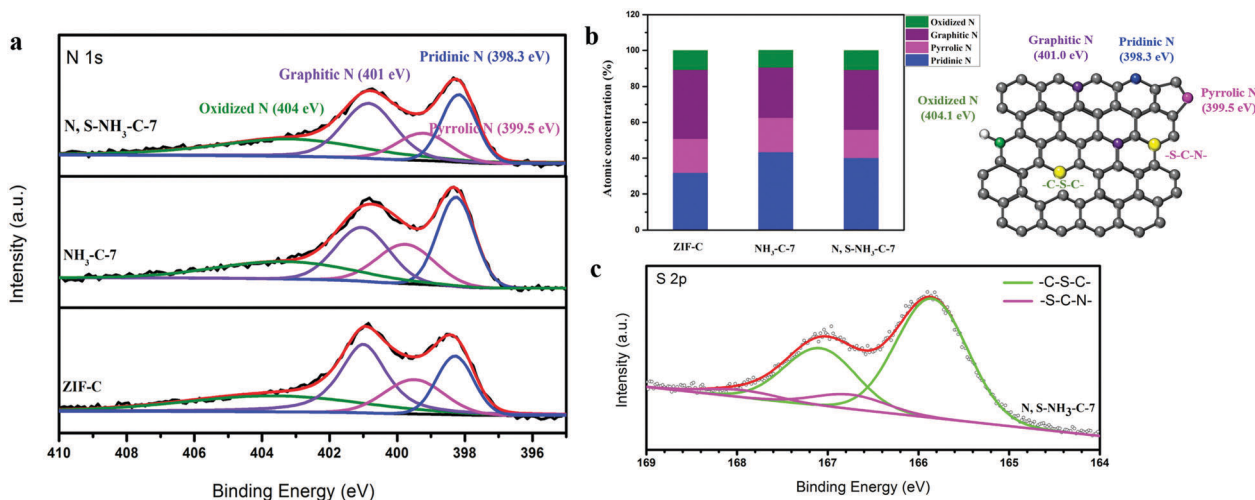


Fig. 5 Chemical binding state of the nanocarbons. (a) N1s XPS spectra of N,S-NH₃-C-7, NH₃-C-7 and ZIF-C. (b) Bar diagrams representing the atomic concentration of four kinds of nitrogen species (left); atomic structure of the N,S-doped nanocarbon with chemical bonding configurations of nitrogen and sulfur dopants (right). (c) S2p XPS spectra of N,S-NH₃-C-7.

possess a 3D structure, are inactive toward ORR. Therefore, the N,S-NH₃-C-7 and NH₃-C-7 nanocarbons which contain more planar pyridinic-N atoms than ZIF-C, are considered to have higher ORR activity. High resolution S2p spectra of N,S-NH₃-C-7 are shown in Fig. 5(c). Due to spin-orbit coupling, signals originating from sulfur atoms are represented as a doublet. The S2p spectra of N,S-NH₃-C-7 reveal two major chemical bonding structures: one from C-S-C chemical bonding located at a low binding energy (165.8–167.1 eV), and another one at a slightly higher binding energy (166.8–168.0 eV) ascribed as -S-C-N-. Since N is more electronegative than S, it is going to hog the electrons in a covalent bond with S, which lead to a more electropositive configuration for S. Therefore, the electronic-insufficient S atoms in the -S-C-N- chemical environment display a signal that is red shifted to a higher binding energy. These two different S chemical environments of C-S-C and -S-C-N- should exhibit different catalytic activities toward ORR. The -S-C-N- bonding structure, in which N and S are close to each other and doped on the same C atom, is expected to be the more active doping site for ORR. To prove this speculation, further catalytic activity toward ORR of the nanocarbon electrocatalyst and the first-principles calculations is provided below.

The electrochemical performance of the as-prepared nanocarbons toward ORR is analyzed and compared with their counterparts (NH₃-C-*x*, ZIF-C, and the commercial catalyst Pt/C). CV measurements of N,S-NH₃-C-7 in N₂-saturated and O₂-saturated 0.1 M KOH electrolytes are presented, respectively, in Fig. 6(a). Compared to the featureless CV curves obtained in the N₂-saturated electrolyte, a distinct oxygen reduction peak is observed at ~ -0.18 V (*vs.* Ag/AgCl) in O₂-saturated KOH solution, indicating the ORR catalytic activity for the N,S-NH₃-C-7 nanocarbon. Fig. 6(b) presents the LSV curves of the nanocarbon catalysts obtained in an O₂-saturated 0.1 M KOH electrolyte at a rotating speed of 1600 rpm. According to the analysis of the electrochemical performance, NH₃-C-7 displays a higher ORR

half-wave potential ($E_{1/2} = -0.194$ V) and an increased limiting current density ($I_{lim} = 3.59$ mA cm⁻²) compared to ZIF-C ($E_{1/2} = -0.286$ V, $I_{lim} = 2.80$ mA cm⁻²). This indicates that the catalytic activity of the nanocarbons can be enhanced *via* NH₃ treatment. In addition, extension of the NH₃ treatment time of ZIF-C increases the catalytic activity of the nanocarbons. As shown in Fig. S5 (ESI[†]), NH₃-C-7 shows a better catalytic activity compared to NH₃-C-3 and NH₃-C-5. The good performance is embodied in the elevated limiting current density of NH₃-C-7 and a 90 mV positively shifted half-wave potential compared to NH₃-C-3. The excellent electrochemical performance of NH₃-C-7 compared to ZIF-C confirms the significance of tuning the mesoporous structure of the nanocarbon in promoting the ORR performance. After co-doping S atoms into the NH₃-C-7 nanocarbon, the nanocarbon of N,S-NH₃-C-7 shows the most positive-shifted half-wave potential of $E_{1/2} = -0.13$ V. A half-wave potential is much higher than that of ZIF-C and NH₃-C-7 and comparable to that of the Pt/C catalyst ($E_{1/2} = -0.12$ V). Moreover, the N,S-NH₃-C-7 nanocarbon has an enhanced limiting current density of 3.99 mA cm⁻², a current density which is higher than that for NH₃-C-7 (3.59 mA cm⁻²) and Pt/C (3.75 mA cm⁻²). These results confirm that the enhanced ORR activity can be realized in the N,S-co-doped nanocarbon system. To prove the combination of NH₃ treatment and N,S-co-doping is necessary for the catalyst design, the nanocarbon of N,S-ZIF-C with only N,S-co-doping of ZIF-C but no NH₃ treatment is prepared. By analysis of the electrochemical performance of N,S-ZIF-C toward ORR, it shows that the N,S-ZIF-C nanocarbon exhibits improved activity compared to ZIF-C. However, the half-wave potential ($E_{1/2} = -0.192$ V) and the limiting current (3.20 mA cm⁻²) are much lower than those of the N,S-NH₃-C-7 catalyst. It is supposed that the poor performance is due to the microporous structure of N,S-ZIF-C. The small size of the micropore is difficult for the reactants diffusion, which will increase the mass transport resistance and impact the ORR activity. To further investigate the ORR kinetics of the N,S-NH₃-C-7

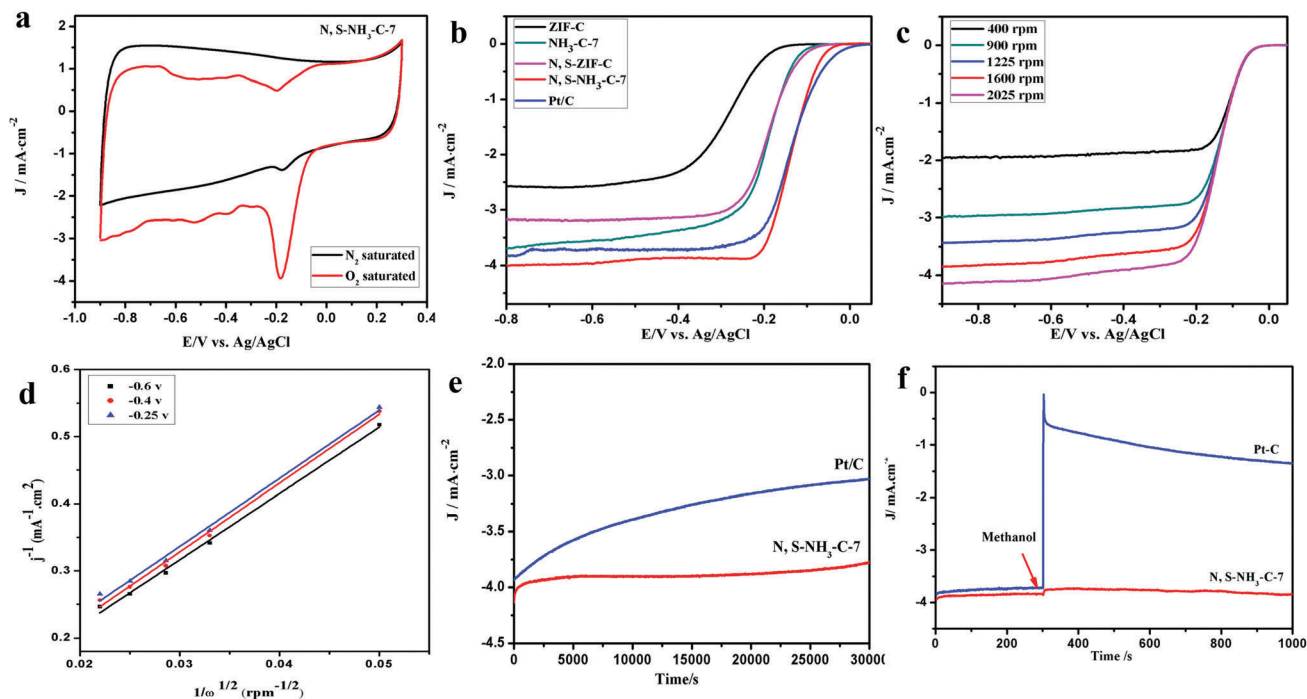


Fig. 6 (a) Cyclic voltammograms of N,S-NH₃-C-7 with a scan rate of 10 mV s⁻¹ in O₂-saturated (red) and N₂-saturated (black) 0.1 M KOH solution. (b) Linear sweep voltammograms (LSVs) of ZIF-C (black), NH₃-C-7 (blue), N,S-NH₃-C-7 (red), and 20% Pt/C (cyan) in O₂-saturated 0.1 M KOH solution at 1600 rpm with a scan rate of 10 mV s⁻¹ after background subtraction. The LSV curves for NH₃-C-x are shown in Fig. S5 (ESI†). (c) LSV curves of N,S-NH₃-C-7 in O₂-saturated 0.1 M KOH with various rotation speeds at a scan rate of 10 mV s⁻¹. The corresponding Koutecky–Levich plots at various voltages are shown in (d). (e) Stability (e) and methanol tolerance (f) curves for N,S-NH₃-C-7 and Pt/C catalysts in O₂-saturated 0.1 M KOH at 1600 rpm with a scan rate of 10 mV s⁻¹.

catalyst, LSV polarization curves are generated using a rotating disc electrode. The tests are conducted at a variety of rotating speeds ranging from 400 to 2025 rpm, and the kinetic parameters are analyzed using the Koutecky–Levich (K–L) equation. In Fig. 6(c and d), the K–L plots of the N,S-NH₃-C-7 nanocarbon at -0.25 V, -0.4 V and -0.6 V exhibit good linearity and parallelism, indicating the presence of the first-order reaction kinetics in regard to the oxygen concentration, and a similar electron transfer number (n) toward ORR at various potentials. The values of n for N,S-NH₃-C-7, calculated from the slope of K–L plots, vary from 3.49 to 3.81 in the potential range of -0.6 V to -0.25 V. This means that the ORR process takes place in a four-electron pathway.

The long-term durability is crucial for evaluating the performance of a new electrocatalyst. The durability of the N,S-NH₃-C-7 nanocarbon and the commercial Pt/C catalyst is analyzed at -0.4 V (*vs.* Ag/AgCl) in O₂-saturated 0.1 M KOH at 1600 rpm over 30 000 s of continuous operation. It is observed that the N,S-NH₃-C-7 catalyst is more stable than the commercial Pt/C catalyst (Fig. 6(e)). The current density of N,S-NH₃-C-7 changed from 4.03 mA cm⁻² to 3.70 mA cm⁻² with only 8.2% loss after the long-time durability testing, while a higher current density loss of 22.6% is observed for the Pt/C catalyst. Besides the excellent durability, the N,S-NH₃-C-7 catalyst also displays an excellent immunity towards methanol crossover reactions, which overcomes another disadvantage faced by the Pt/C catalyst. 1.0 M of methanol is added into a 0.1 M KOH electrolyte solution to investigate methanol tolerance for the N,S-NH₃-C-7 nanocarbon and the Pt/C catalyst (Fig. 6(f)). It was found that methanol injection causes

a sharp current decrease for the Pt/C catalyst, while it has almost no influence on the N,S-NH₃-C-7 nanocarbon, proving an excellent ORR selectivity and a good performance for methanol tolerance.

To understand the intrinsic ORR catalytic mechanism of the N,S-doping effect, first-principles calculations are carried out to determine the electronic structure and the catalytic reaction for the N-doped nanocarbon (Fig. 7(a)) and the N,S-co-doped nanocarbon. In the co-doped structure, N and S may exist within a framework in a variety of configurations, including N,S-isolated dopants (Fig. 7(b)), and N,S-coupled dopants (in which N and S are close to each other and doped on the same C atom) (Fig. 7(c)). The calculated free energy profiles, according to equations (1)–(5) (ESI†), on these three structures are shown in Fig. 7(d–f), respectively. The corresponding intermediate configurations are shown in Fig. S6(a–l) (ESI†). In Fig. 7(d–f), the free energy of each reaction (ΔG) is downhill for the first several steps, except for OH* + e⁻ → OH⁻ + *, which is thermodynamically uphill (endothermic). This result suggests that the reduction of OH* into OH⁻ is the rate determining step for the ORR process. As the overpotential of the ORR is an important measure of the activity of a catalyst, we calculated the overpotential for each active site and determined the minimum overpotential for ORR on the doped structures. Thermodynamically, a lower overpotential means better catalytic activity. The N-doped, isolated N,S-doped, and N,S-coupled carbon structures are identified to have minimum ORR overpotentials of 0.403 V, 0.270 V, and -0.004 V at the electrode potential of 0 V, respectively. Obviously, the N,S-co-doped nanocarbon with

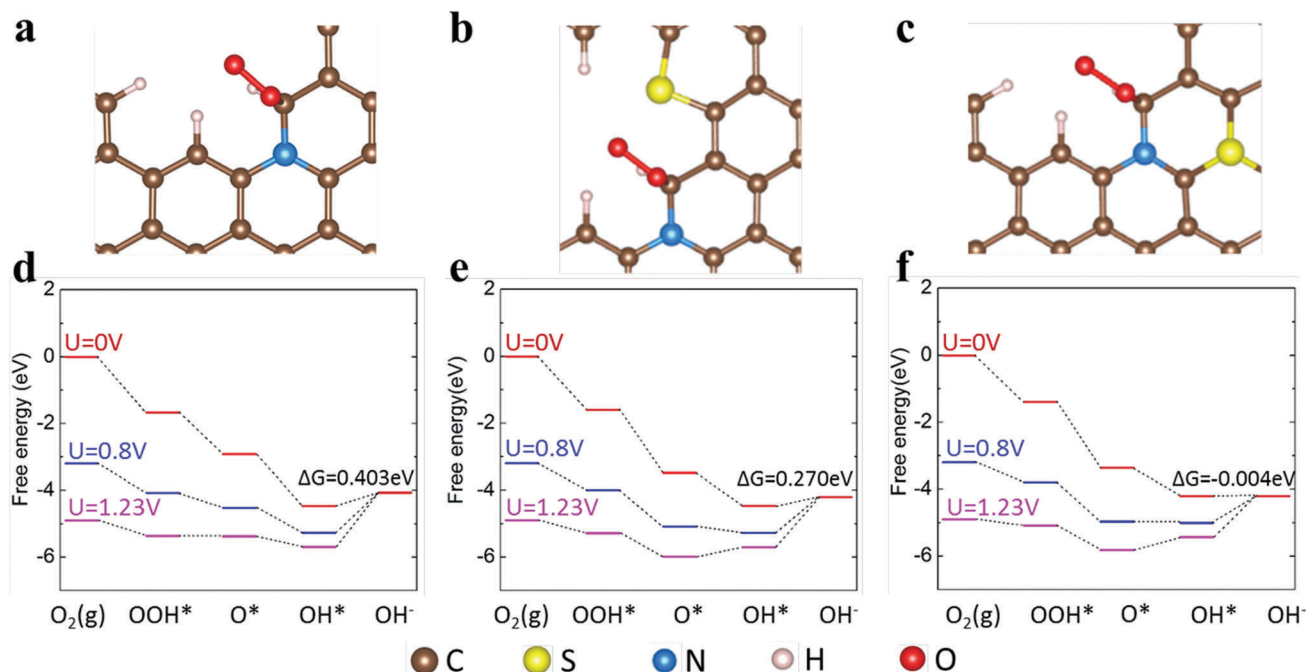


Fig. 7 Optimized structures for the stable adsorbed O_2 on the N-doped nanocarbon (a), the N,S-isolated nanocarbon (b) and the N,S-coupled nanocarbon (c). Free-energy diagram of the ORR on the N-doped nanocarbon (d), the N,S-isolated nanocarbon (e) and the N,S-coupled nanocarbon (f) in alkaline media. The * denotes the adsorption on the surface.

N,S-coupled dopants has the lowest overpotential and exhibits the best catalytic activity toward ORR.

As we know, the ORR reaction process has a close relationship with the charge transfer reaction between the adsorbates and the substrate. Taking O_2 adsorption as an example, the Bader charge⁴⁵ of the O_2 adsorbed on the corresponding doping structures has been studied. As shown in Table S1 (ESI[†]), the Bader charges of O_2 adsorption on the N-doped nanocarbon, the N,S-isolated nanocarbon and the N,S-coupled nanocarbon, are 12.58, 13.19, and 13.30, respectively. The N,S-coupled nanocarbon, in which N and S atoms are close to each other, could provide a greater electron density to the adsorbed O_2 as opposed to the other two structures, making O_2 and its related species more active. This is the synergistic effect arising from N and S dopants. The synergistic effect of N,S-coupled dopants leads to more active sites of carbon and therefore enhances the ORR activity of the nanocarbon. Thus first-principles calculations prove that N,S-coupled dopants create active sites with a higher activity than the isolated N and S dopants. It is, for the first time, to pinpoint the doping-active sites, with solid evidences, which is a key factor to determine the performance of the nanocarbon catalyst. The discovery on the doping structure–performance relationship of the nanocarbon provides guidelines for the design of novel electrocatalysts with a high activity.

Conclusions

A novel N,S-co-doped nanocarbon electrocatalyst derived from a MOF of ZIF-8 has been developed. It is found that compared to the noble-metal Pt/C catalyst, the N,S-co-doped nanocarbon

exhibits excellent catalytic activity and long-term stability toward ORR in alkaline media. The high specific surface area and appropriate porosity built in the N,S-co-doped nanocarbon are beneficial for the mass transportation and facilitate the ORR process. More importantly, first-principles calculations reveal that the N,S-coupled dopants promote the carbon sites with a higher activity compared to the isolated N and S dopants. The N,S-coupled nanocarbon provides a great electron density to the adsorbed O_2 , thus making O_2 and its species to be reduced. The highly active co-doping sites resulting from the synergistic effect well explain the origin of the enhanced ORR activity for the N,S-co-doped nanocarbon. The approach and analysis adopted in this work offer a strategic consideration for designing the high performance nanocarbon electrocatalyst.

Acknowledgements

This research was supported by the Natural Sciences and Engineering Research Council of Canada (NSERC), the Canada Research Chair (CRC) Program, the Canada Foundation for Innovation (CFI), the Ontario Research Fund (ORF), the Canadian Light Source (CLS), the McMaster National Microscopy Centre, and the University of Western Ontario. Z. Song was supported by the Chinese Scholarship Council (CSC). L. L. M. was supported by the National Natural Science Foundation of China (NSFC) (grant no. 51572016 and U1530401). The computational support from a Tianhe-2 JK computing time at the Beijing Computational Science Research Center (CSRC) is also acknowledged.

Notes and references

- 1 M. K. Debe, *Nature*, 2012, **486**, 43–51.
- 2 G. Wu and P. Zelenay, *Acc. Chem. Res.*, 2013, **46**, 1878–1889.
- 3 B. C. H. Steele and A. Heinzl, *Nature*, 2001, **414**, 345–352.
- 4 P. Chen, T.-Y. Xiao, Y.-H. Qian, S.-S. Li and S.-H. Yu, *Adv. Mater.*, 2013, **25**, 3192–3196.
- 5 N. Cheng, M. Norouzi Banis, J. Liu, A. Riese, S. Mu, R. Li, T.-K. Sham and X. Sun, *Energy Environ. Sci.*, 2015, **8**, 1450–1455.
- 6 N. Cheng, M. N. Banis, J. Liu, A. Riese, X. Li, R. Li, S. Ye, S. Knights and X. Sun, *Adv. Mater.*, 2015, **27**, 277–281.
- 7 B. Lim, M. Jiang, P. H. Camargo, E. C. Cho, J. Tao, X. Lu, Y. Zhu and Y. Xia, *Science*, 2009, **324**, 1302–1305.
- 8 V. Mazumder, M. Chi, K. L. More and S. Sun, *J. Am. Chem. Soc.*, 2010, **132**, 7848–7849.
- 9 L. Yang, M. B. Vukmirovic, D. Su, K. Sasaki, J. A. Herron, M. Mavrikakis, S. Liao and R. R. Adzic, *J. Phys. Chem. C*, 2013, **117**, 1748–1753.
- 10 N. Cheng, S. Stambula, D. Wang, M. N. Banis, J. Liu, A. Riese, B. Xiao, R. Li, T.-K. Sham, L.-M. Liu, G. A. Botton and X. Sun, *Nat. Commun.*, 2016, **7**, 13638.
- 11 W. Ding, L. Li, K. Xiong, Y. Wang, W. Li, Y. Nie, S. Chen, X. Qi and Z. Wei, *J. Am. Chem. Soc.*, 2015, **137**, 5414–5420.
- 12 W. Niu, L. Li, X. Liu, N. Wang, J. Liu, W. Zhou, Z. Tang and S. Chen, *J. Am. Chem. Soc.*, 2015, **137**, 5555–5562.
- 13 D. Geng, Y. Chen, Y. Chen, Y. Li, R. Li, X. Sun, S. Ye and S. Knights, *Energy Environ. Sci.*, 2011, **4**, 760–764.
- 14 X. Liu, L. Li, W. Zhou, Y. Zhou, W. Niu and S. Chen, *ChemElectroChem*, 2015, **2**, 803–810.
- 15 K. Gong, F. Du, Z. Xia, M. Durstock and L. Dai, *Science*, 2009, **323**, 760–764.
- 16 R. Liu, D. Wu, X. Feng and K. Müllen, *Angew. Chem.*, 2010, **122**, 2619–2623.
- 17 G. Wu, K. L. More, C. M. Johnston and P. Zelenay, *Science*, 2011, **332**, 443–447.
- 18 L. Yang, S. Jiang, Y. Zhao, L. Zhu, S. Chen, X. Wang, Q. Wu, J. Ma, Y. Ma and Z. Hu, *Angew. Chem.*, 2011, **123**, 7270–7273.
- 19 S. Inamdar, H.-S. Choi, P. Wang, M. Y. Song and J.-S. Yu, *Electrochem. Commun.*, 2013, **30**, 9–12.
- 20 Z. W. Liu, F. Peng, H. J. Wang, H. Yu, W. X. Zheng and J. Yang, *Angew. Chem.*, 2011, **123**, 3315–3319.
- 21 D.-S. Yang, D. Bhattacharjya, S. Inamdar, J. Park and J.-S. Yu, *J. Am. Chem. Soc.*, 2012, **134**, 16127–16130.
- 22 J. Zhang, Z. Zhao, Z. Xia and L. Dai, *Nat. Nanotechnol.*, 2015, **10**, 444–452.
- 23 W. Yang, T.-P. Fellingner and M. Antonietti, *J. Am. Chem. Soc.*, 2010, **133**, 206–209.
- 24 N. Ranjbar Sahraie, J. P. Paraknowitsch, C. Göbel, A. Thomas and P. Strasser, *J. Am. Chem. Soc.*, 2014, **136**, 14486–14497.
- 25 X. Gong, S. Liu, C. Ouyang, P. Strasser and R. Yang, *ACS Catal.*, 2015, **5**, 920–927.
- 26 M. Zhang and L. Dai, *Nano Energy*, 2012, **1**, 514–517.
- 27 W. Yang, X. Yue, X. Liu, J. Zhai and J. Jia, *Nanoscale*, 2015, **7**, 11956–11961.
- 28 W. Kiciński, M. Szala and M. Bystrzejewski, *Carbon*, 2014, **68**, 1–32.
- 29 M. Fujita, Y. J. Kwon, S. Washizu and K. Ogura, *J. Am. Chem. Soc.*, 1994, **116**, 1151–1152.
- 30 Y. Zhao, Z. Song, X. Li, Q. Sun, N. Cheng, S. Lawes and X. Sun, *Energy Storage Mater.*, 2016, **2**, 35–62.
- 31 W. Chaikittisilp, K. Ariga and Y. Yamauchi, *J. Mater. Chem. A*, 2013, **1**, 14–19.
- 32 Z. Song, N. Cheng, A. Lushington and X. Sun, *Catalysts*, 2016, **6**, 116.
- 33 Q. L. Zhu, W. Xia, T. Akita, R. Zou and Q. Xu, *Adv. Mater.*, 2016, **28**, 6391–6398.
- 34 A. Mahmood, W. Guo, H. Tabassum and R. Zou, *Adv. Energy Mater.*, 2016, **6**, DOI: 10.1002/aenm.201600423.
- 35 L. Zhang, Z. Su, F. Jiang, L. Yang, J. Qian, Y. Zhou, W. Li and M. Hong, *Nanoscale*, 2014, **6**, 6590–6602.
- 36 F. Zheng, Y. Yang and Q. Chen, *Nat. Commun.*, 2014, **5**, 5261.
- 37 Y. Lv, F. Zhang, Y. Dou, Y. Zhai, J. Wang, H. Liu, Y. Xia, B. Tu and D. Zhao, *J. Mater. Chem.*, 2012, **22**, 93–99.
- 38 L. Sun, C.-I. Wang, Y. Zhou, X. Zhang and J.-s. Qiu, *Carbon*, 2014, **71**, 344–345.
- 39 X. Yang, G. Zhang, M. Zhong, D. Wu and R. Fu, *Langmuir*, 2014, **30**, 9183–9189.
- 40 X. Li, Q. Sun, J. Liu, B. Xiao, R. Li and X. Sun, *J. Power Sources*, 2016, **302**, 174–179.
- 41 M. V. Ivanova, C. Lamprecht, M. J. Loureiro, J. T. Huzil and M. Foldvari, *Int. J. Nanomed.*, 2012, **7**, 403–415.
- 42 N. Cheng, Y. Shao, J. Liu and X. Sun, *Nano Energy*, 2016, **29**, 220–242.
- 43 Q. Wang, W. Xia, W. Guo, L. An, D. Xia and R. Zou, *Chem. – Asian J.*, 2013, **8**, 1879–1885.
- 44 D. Guo, R. Shibuya, C. Akiba, S. Saji, T. Kondo and J. Nakamura, *Science*, 2016, **351**, 361–365.
- 45 E. Sanville, S. D. Kenny, R. Smith and G. Henkelman, *J. Comput. Chem.*, 2007, **28**, 899–908.